

Nature-Inspired Stalactite Nanopores for Biosensing and Energy Harvesting

Andrey Chernev,* Yunfei Teng,* Mukeshchand Thakur, Victor Boureau, Lucie Navratilova, Nianduo Cai, Tzu-Heng Chen, Liping Wen, Vasily Artemov, and Aleksandra Radenovic*

Nature provides a wide range of self-assembled structures from the nanoscale to the macroscale. Under the right thermodynamic conditions and with the appropriate material supply, structures like stalactites, icicles, and corals can grow. However, the natural growth process is time-consuming. This work demonstrates a fast, nature-inspired method for growing stalactite nanopores using heterogeneous atomic deposition of hafnium dioxide at the orifice of templated silicon nitride apertures. The stalactite nanostructures combine the benefits of reduced sensing region typically for 2-dimensional material nanopores with the asymmetric geometry of capillaries, resulting in ionic selectivity, stability, and scalability. The proposed growing method provides an adaptable nanopore platform for basic and applied nanofluidic research, including biosensing, energy science, and filtration technologies.

sequencing,^[1] energy harvesting and generation,^[2,3] bio-inspired iontronics,^[4–6] biosensing,^[7] chemical separation,^[8,9] and nanofluidics.^[10] In particular, there has been growing interest in combining the features of biological pores and channels with the flexibility and robustness of solid-state material membranes that can be fabricated using state-of-the-art technologies.^[11,12] The various applications require the pores to be adjustable, ion-selective, scalable, stable, and affordable.^[7] Currently, the main problems affecting most of the nanopore applications include limited lifetime and instability of the pores,^[13–16] difficulties with wide-range pore-size variation,^[17] limited ion and molecular selectivity, and limited scalability

from single pores to large-scale arrays.^[18] Previous experimental and theoretical studies extensively addressed the challenges of nanopore scalability to create the nanoporous arrays,^[19] and the role of asymmetry that predicted^[20] to provide additional benefits for biosensing and power generation.^[21] The geometrical asymmetry suggests a gradient of electrical potential along the pore axis, which interferes with the external electric field and creates an electrostatic barrier different for positive and negative ions, allowing ionic rectification and molecular separation by sign, charge, and size. These properties particularly provide good conditions for the application of such pores for energy harvesting, biomolecule analysis, and filtration. However, the robust fabrication method of arrays of nanopores with high asymmetry, low resistivity, and scalability remains elusive.

Here, we introduce asymmetric conical nanopores, termed stalactite pores, with unique structures compared to existing solid-state nanopores. The fabrication method of stalactite-nanopores is directly inspired by nature. Myriads of examples exist when periodic thermodynamic conditions permit peculiar structures such as corals, stalactites, brinicles, and icicles.^[22] These naturally assembled objects' structures are formed due to cyclical supplies of precursors and changes in the thermodynamic parameters at the point of growth. This strategy inspired us to use a similar approach applied to nanopores. Unlike natural objects, we used state-of-the-art cleanroom techniques to facilitate the process and dramatically improve its pace. Using the templated silicon nitride (SiN) aperture as a starting point of the growth, we demonstrate the heterogeneous-anisotropic growth of periodic hafnium-oxide rings, resulting in shallow conical ladder-shaped stalactite nanostructures (Figure 1). This fabrication method

1. Introduction


Nature-inspired and artificial nanopores hold great potential in a wide range of applications, such as single-molecule biomolecules

A. Chernev, Y. Teng, M. Thakur, N. Cai, T.-H. Chen, V. Artemov, A. Radenovic
Laboratory of Nanoscale Biology
Ecole Polytechnique Fédérale de Lausanne
Lausanne 1015, Switzerland
E-mail: andrey.chernev@epfl.ch; yunfei.teng@epfl.ch; aleksandra.radenovic@epfl.ch

V. Boureau, L. Navratilova
Interdisciplinary Centre for Electron Microscopy
Ecole Polytechnique Fédérale de Lausanne
Lausanne 1015, Switzerland

L. Wen
CAS Key Laboratory of Bio-Inspired Materials and Interfacial Science
Technical Institute of Physics and Chemistry
Chinese Academy of Sciences
Beijing 100190, P. R. China

L. Wen
School of Future Technology
University of Chinese Academy of Sciences
Beijing 100049, P. R. China

 The ORCID identification number(s) for the author(s) of this article can be found under <https://doi.org/10.1002/adma.202302827>

© 2023 The Authors. Advanced Materials published by Wiley-VCH GmbH. This is an open access article under the terms of the Creative Commons Attribution License, which permits use, distribution and reproduction in any medium, provided the original work is properly cited.

DOI: 10.1002/adma.202302827

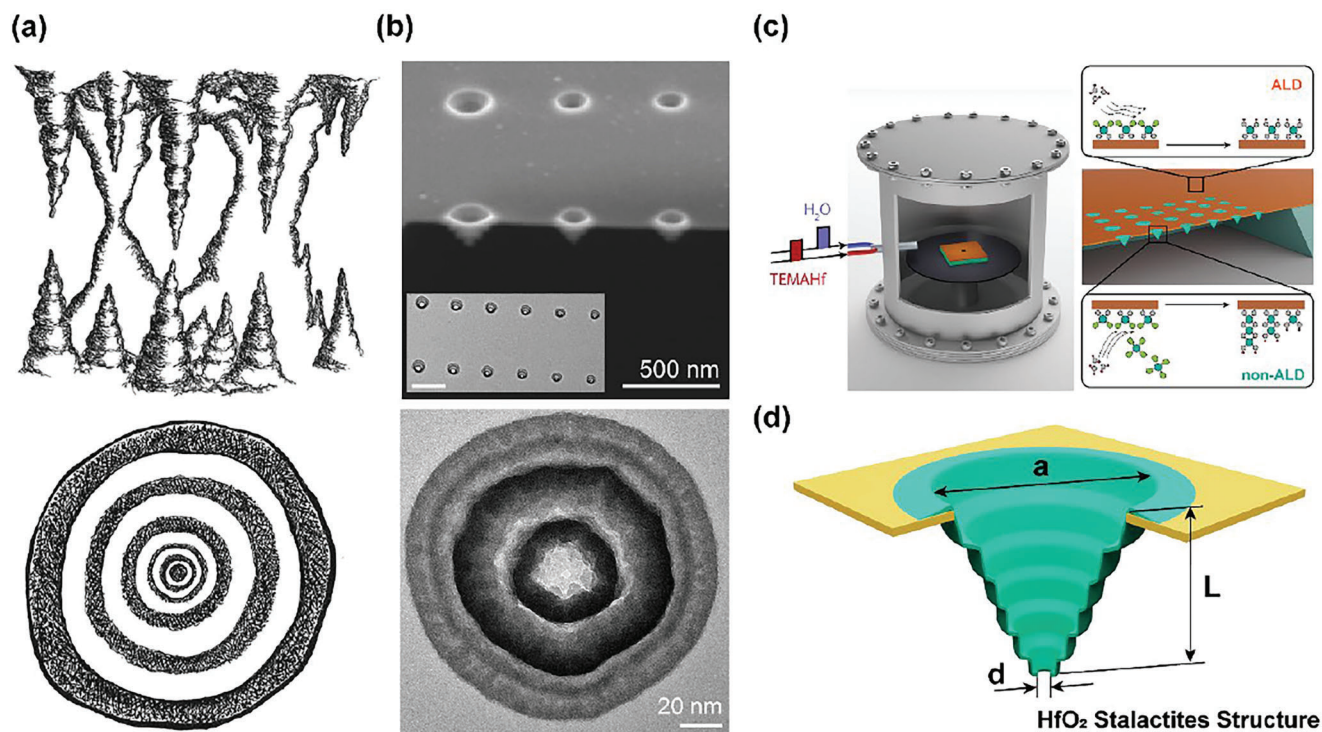


Figure 1. Natural and nature-inspired stalactite nanostructures. a) Stalactites and stalagmites: Artist's representation of the natural formations created by using periodic thermodynamic conditions and material supply (top). The stalactite cross-section schematic (bottom): rings correspond to the growth cycles. b) Electron microscopy (EM) micrographs of HfO_2 stalactite nanopores on the templated silicon nitride apertures obtained in this study: scanning electron microscopy (SEM) side-view image (top), and the high-resolution transmission electron microscopy (TEM) top-view image of a single nanopore (bottom) that is similar to the stalactite periodic structure. The inset shows the TEM image of several nanopores. Scale bar, 500 nm. c) The growth procedure consists of the regular ALD and the selective templated aperture growth. d) Schematic 3D view of the stalactite nanopore. Arrows show variable dimensions of the nanopore.

allows one to create highly asymmetric nanopores with a pore size from single-digit to hundreds of nanometers by tuning the growth parameters and templates, providing a new platform for nanofluidic research with potential for scalability.

2. Experimental

Typical stalactites and stalagmites are structures determined by the precipitation of calcium carbonate from the liquid flowing or dropping on their surfaces (Figure 1a). The combination of material precipitation, fluid dynamics, evaporation, and periodic thermodynamic conditions determines the growth and shape of natural stalactites and stalagmites.^[23] To implement the natural process in artificial nanopore growth, we used templated SiN apertures (Figures S1 and S2, Supporting Information), which were pre-patterned with electronic-beam lithography and dry etching to form periodic templated apertures (Figure 1b inset). We used various templates with a single pore or a multipore array of the same size or gradient aperture size. To realize the stalactite structures at the nanoscale (Figure 1b), the templated SiN apertures were placed into the chamber, typically used for atomic-layer deposition (ALD) (Figure 1c), yet the growth regimes were different.

Adapting the standard ALD process, the precursors, namely water vapor and tetrakis-(ethylmethylamido)-hafnium (IV), were used for HfO_2 growth, varying the pulse duration. Templated SiN

aperture on a single chip substrate served as a nanoreactor for the material precipitation (Figure 1c). Due to the heterogeneity of the substrate caused by the presence of aperture(s) and presumably due to the local concentration gradients of precursors, precipitation was mainly at the orifice of the aperture(s). The growth rate at the aperture orifice was two orders of magnitude higher than the aperture-free region. As a result, HfO_2 stalactite nanopores were forming at each aperture (Figure 1d), presumably because the precursor molecules have not had enough time to diffuse away from being trapped by the compartment formed by the aperture and resulted in the chemical vapor deposition (CVD)-like growth. When the time between the pulses was increasing, molecules had sufficient time to diffuse, and the standard ALD growth mode took place (Figures S3 and S4, Supporting Information).

3. Results

The typical stalactite HfO_2 nanopore is shown in the transmission electron microscopy (TEM) micrograph in Figure 1b. The pore array is shown on top, and the single pore is enlarged on the bottom, where the gray-and-black contrast demonstrates the periodic structure of the pore. Each ring corresponds to one growth cycle. Each pore has a 3D structure. The 3D sketch of a single pore is shown in Figure 1d. The pore has a conical shape of the length L , defined by the number of rings. The pore base diameter

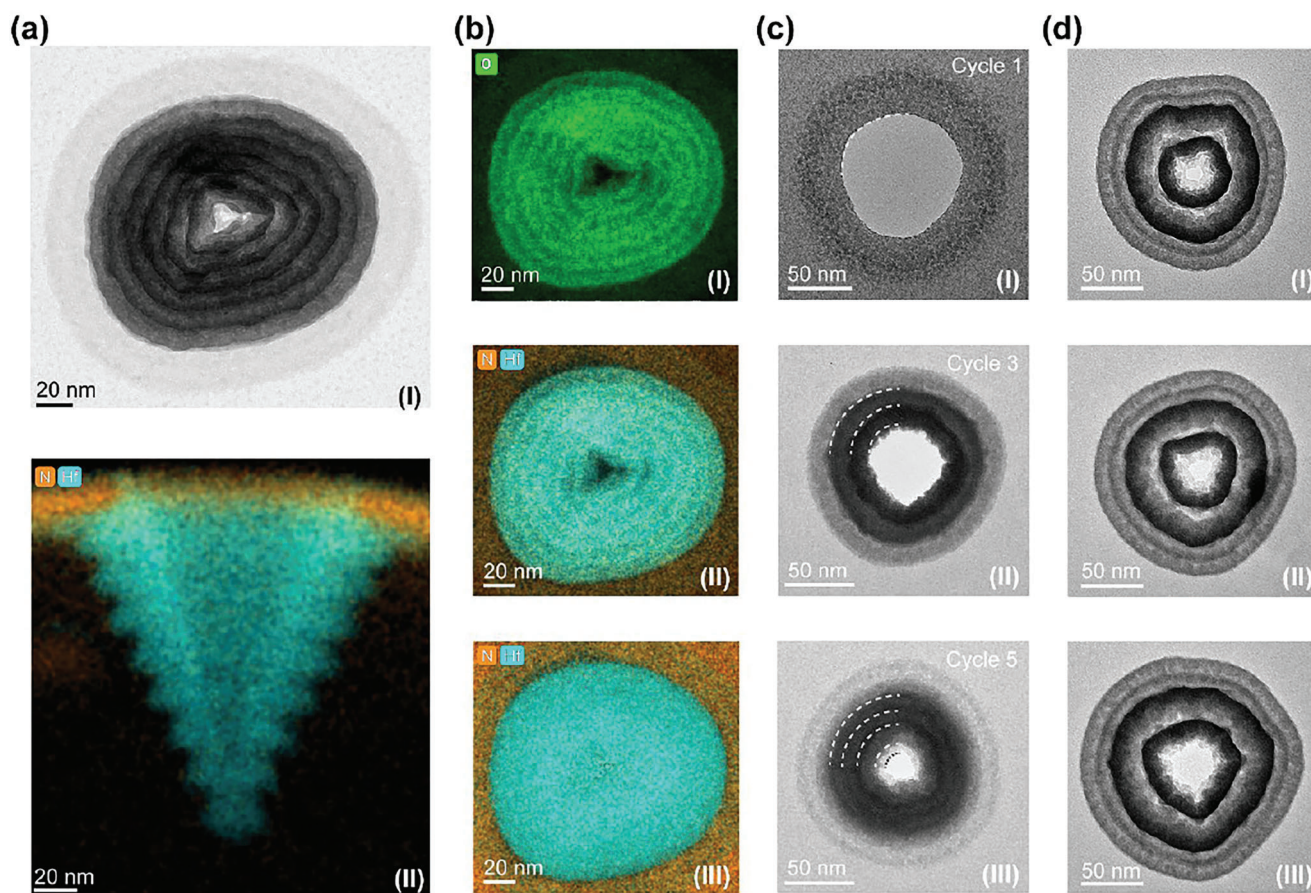


Figure 2. Transmission electron microscopy (TEM) imaging of a single stalactite nanopore. a) High-resolution top-view TEM image (I). The corresponding energy-dispersive X-ray (EDX) side-view mapping (II). Cyan and orange colors are for hafnium and nitrogen signals, respectively. b) The EDX top-view mapping of stalactite nanopore, corresponding to the net count signal of O (I), combining the net count signal of Hf and N (II) and an atomic fraction (normalized signal) of Hf and N (III). c) TEM image of the pore after one (I), three (II), and five (III) growth cycles. The dashed curves are guides for the eye. d) TEM micrographs of the pore with the initial aperture diameter of 100 (I), 120 (II), and 150 (III) nm.

a is defined by the initial aperture diameter. The pore tip diameter d depends on the number of cycles and can be as low as 3 nm (Figure 1b bottom).

TEM images, including energy-dispersive X-ray (EDX) mapping, are shown in Figure 2. The TEM micrograph (Figure 2a(I)) shows that a single HfO_2 stalactite has a periodic step-like structure similar to that observed in natural stalactites (Figure 1a). The pore shown on the picture has eight rings. The rings grow in the direction from the pore perimeter to the center so that a preceding ring is a template for the next ring with a gradually reducing diameter. The EDX spectroscopy analysis of the side-view projection prepared with a focused ion beam shows the elemental composition of the stalactite (Figure 2a(II)). The signal from hafnium atoms (cyan) corresponds to the stalactite body, whereas nitrogen atoms (orange) correspond to the silicon nitride membrane. Figure 2b(I) shows that the shape of the step-like structure follows the EDX signal of oxygen in the nano stalactite from the top view and combining hafnium and nitrogen mapping shows the same heterogeneity in the net count signal of Hf (Figure 2b(II)). The step-like structure disappears in the atomic fraction mapping (Figure 2b(III)), indicating the homogeneous distribution of hafnium within the stalactite.

There are two ways of tuning the pore diameter. The first is choosing the number of growth cycles (Figure 2c). For example, one, three, and five cycles result in zero, two, and four rings in the HfO_2 stalactite nanostructure, respectively. Therefore, each growth cycle except the first one adds a ring to the stalactite until it clogs. In other words, n cycles of precursor supply result in $n-1$ rings. The second way to control the stalactite dimensions is by varying the diameter of the templated silicon-nitride apertures (Figure 2d). The decrease in the aperture diameter results in smaller nanopores for the same number of growth cycles. The fine-tuning of the growth cycles and choosing the apertures' diameter allows to obtain the stalactite nanopore with desired dimensions (Figure 1d). Careful adjustment of the growth parameters prevents the overgrowth of the stalactite nanostructure and the consequent termination of the nanopore due to the overflowing of its inner volume.

3.1. Stalactite Nanopore in Nanofluidic Experiments

A distinctive feature of the stalactite nanopore is its asymmetry. The latter studies demonstrated how the charge and mass

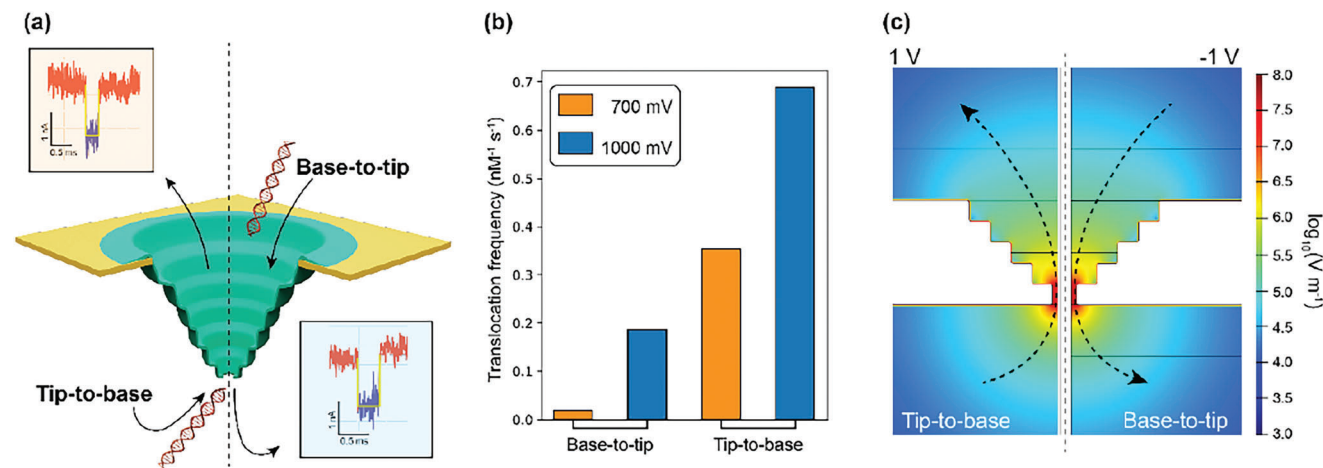


Figure 3. Single stalactite nanopore as a biosensor. a) Experimental layout for tip-to-base and base-to-tip directions for DNA translocation. Insets show current traces of translocation events. b) Concentration-normalized DNA translocation frequency in two directions as a function of applied voltage. c) Nonuniform electric field intensity distribution inside the pore (log scale). Arrows show the direction of DNA translocation in two principal directions.

transports are affected by the asymmetric structure under different working conditions, including a voltage bias and a concentration gradient.^[24–26] Particularly, the tapering geometry creates nonuniformity of the electric field distribution, helping separate charges and, for example, produce electricity from the concentration gradients^[20] or affecting the translocation rate of the biomolecules through the pore.^[27,28] To understand the impact of the asymmetric geometry on the ionic and molecular transport through the stalactite nanopore and estimate its “efficiency,” we performed DNA translocation and reverse electro dialysis experiments. The latter was made on both a single pore and a nanopore array.

3.2. Biosensing: DNA Translocations

Figure 3a shows a layout for the DNA translocation experiment. The insets demonstrate an electric current through the pore during a single DNA translocation event for two cases: tip-to-base (left) and base-to-tip (right) directions of translocation. The total number of Cumulative Sums (CUSUM)-fitted events used for analysis were 426, 1626, and 2327 events at 500 mV, 700 mV, and 1 V, from tip-to-base direction, two representative events (each direction) are shown in Figure 3a inset and more events are shown in Figure S7 (Supporting Information). The object of interest is the difference in the translocation frequency between two directions with charged DNA driven by an electric field. We used two voltage levels of 0.7 and 1 V. The current–voltage characteristics are given in Figure S5 (Supporting Information), and details of translocation comparison are shown in Figures S6–S9 (Supporting Information).

The asymmetric shape of the pore yields asymmetry in the DNA translocation (Figure 3b). The concentration-normalized DNA translocation rate for the tip-to-base direction is higher than for the base-to-tip direction. This difference is presumably due to the higher translocation energy barrier for the second case caused by the nonuniform electric field distribution^[29] and the electroosmotic flow^[30] that the negatively-charged DNA molecule

overcomes. In our base-to-tip configuration, the first pore opening of 80–100 nm is the first barrier to capture diffusing dsDNA molecule(s) around the pore area. A 2 kbp DNA radius of gyration (R_g) is ≈ 80 –90 nm and a contour length of ≈ 680 nm at 1 M KCl. The DNA must assume a more linear conformation as it approaches the pore while still under an electric field.^[31] The conformational alteration reduces the conformational entropy of the DNA with various possible chain conformations. This could raise the system’s free energy where the DNA can negotiate with various coil deformations. This entropic barrier impedes or restricts the threading process, thereby reducing the translocation efficiency. Further, the molecule once confined inside the HfO₂ stalactite structure, has to funnel through the pore (a second barrier) with a diameter of about 16 nm. Therefore, lower translocation frequency could arise from such high entropic costs involved in the translocation process.

The DNA translocation phenomenon is entropy-dominated at the pore entrance or drift-dominated caused by the electric-field surpassing the entropic effects.^[31,32] For tip-to-base configuration, the translocations were recorded for 3.9, 3.8, and 2.9 min for 500 mV, 700 mV, and 1V, respectively. The estimated DNA translocation frequencies at fixed 20 nm DNA concentration are 0.05, 0.35, 0.68 events s⁻¹ nm⁻¹ at 500 mV, 700 mV, and 1V, respectively. A nonlinear dependence of translocation frequency is observed as a function of voltage in tip-to-base configuration probably due to entropic effects. But a more dedicated study is needed to compare the translocation dynamics at different experimental parameters such as different polymer lengths, polymer concentrations, ion-gradient conditions, and pressure-assisted translocations to elucidate the mechanism of DNA transport behavior in stalactite nanopores in two configurations with perhaps longer time scales. In quartz nanopipettes (≈ 15 nm diameter), with similar sizes as our pore, a nonlinear translocation frequency (≈ 0.6 events s⁻¹ nm⁻¹ at 700 mV) was observed in 4 M LiCl for 2 kbp DNA length.^[29] At the same time, a linear translocation frequency was observed for longer DNA lengths of >5 kbp in 1 M KCl. This variation was attributed to the decrease in the effective charge on DNA by Li⁺ ions compared to K⁺ ions.^[33]

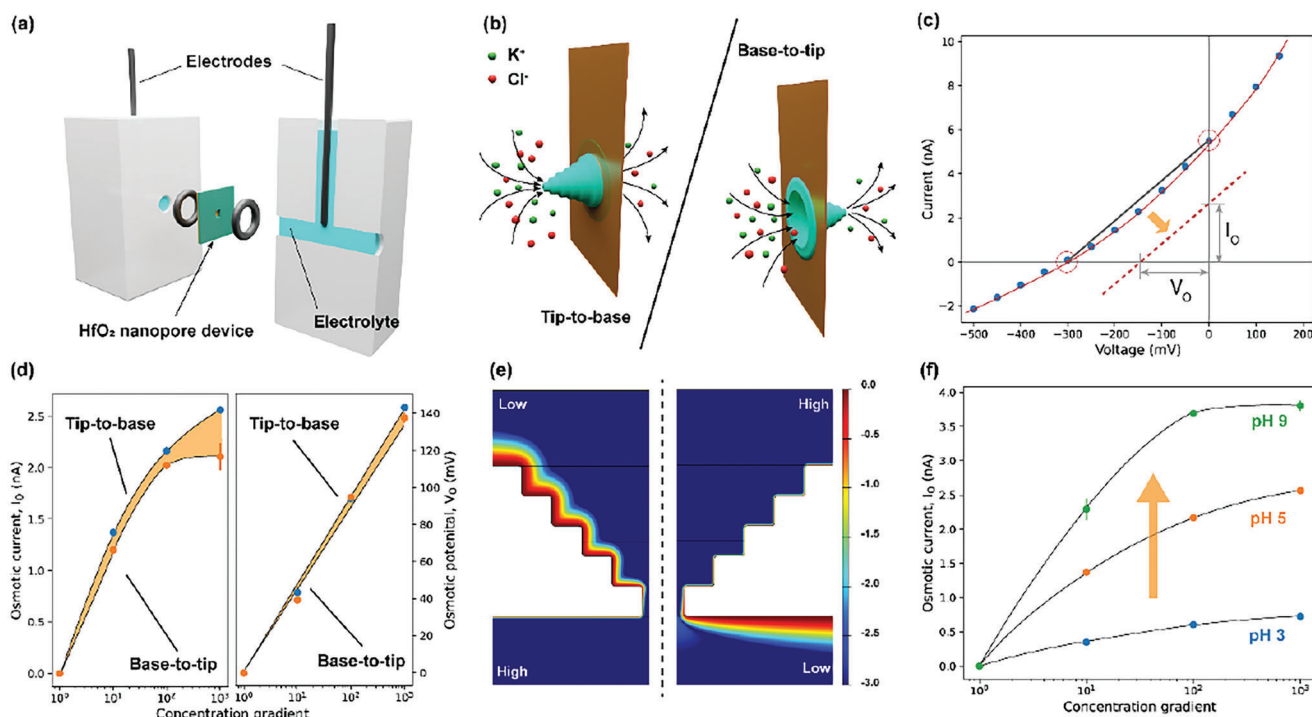


Figure 4. Reversed electrodialysis (RED) experiment on a single stalactite nanopore. a) Setup layout. b) 3D reconstruction of a nanopore. Arrows show the ionic current for tip-to-base (left) and base-to-tip (right) directions. The left side has a higher ion concentration compared to the right side. c) The current-voltage characteristics of the stalactite nanopore for the tip-to-base direction of the 1000-fold concentration gradient at around pH = 5 condition. Lines are guides for the eye. V_o and I_o are osmotic voltage and osmotic current, respectively, calculated according to the previously reported publication.^[39] d) Osmotic current (left) and osmotic voltage (right) at different salt concentration gradients at pH = 5. The gradient is given as a ratio between the concentrations on the opposite sides of the membrane. The orange areas are guides for the eye, indicating the difference between tip-to-base and base-to-tip flow directions. e) Electric charge distribution in the case of tip-to-base (left) and base-to-tip (right) directions of the concentration gradient. f) Osmotic current versus concentration gradient at different pH for the tip-to-base gradient. Black lines are guides for the eye. The arrow shows the pH increase.

Similarly, an asymmetric translocation dynamics have been shown in nanopipettes (≈ 15 nm diameter), where the DNA entry is restricted from the base-to-tip direction and is hindered as the DNA is under tension while the tip-to-base is favorable.^[34] Furthermore, the phosphate groups on DNA tend to interact with HfO_2 surface which could explain longer-dwell time owing to the surface interaction between dsDNA and stalactite pore.^[13,35]

Our COMSOL simulation shows that the pore has an electric field gradient along the symmetry axis (Figure 3c). The nonuniform electric field of the pore increases the chances for the negatively charged DNA molecule to be trapped from the tip side compared to the base side. As the effect has a pure electrostatic nature, we expect the pore asymmetry will affect the translocation of any charged molecules passing through the pore. This effect can be used for biomolecule characterization and separation. We did not observe a significant difference in the passage time of DNA in two directions. Most translocation events in both directions are ≈ 100 – 250 μs (Figure S9, Supporting Information), and the bandwidth further limits the resolution of fast translocations.^[36] The translocation velocity of DNA in conical nanopores has shown differential time scales while DNA enters or exits the nanopore.^[34] As shown in Figure S10 (Supporting Information), the pore displays $1/f$ noise that arise from the fluctuation in the electrical current as a function of time. The origin

noise can arise from various sources such as fluctuations in the charge carriers crowding and interacting with the pore, presence of nanobubbles, local surface charge, or fluctuations in the local electric field.^[37]

3.3. Energy Harvesting: Reverse Electrodes

Asymmetric pores empower energy harvesting. **Figure 4a** shows the schematics of the reverse electrodes experiment aimed to demonstrate the osmotic energy conversion.^[38] The setup consisted of a single stalactite nanopore in the membrane separating two volumes with aqueous KCl solutions. The concentration gradient between the opposite sides of the membrane was changing within three orders of magnitude. Two Ag/AgCl electrodes were used for recording the ionic current. The efficiency of ions rectification was compared for two cases of the tip-to-base and the base-to-tip flow directions (Figure 4b). The experiments were repeated several times using stalactite nanopores with a tip diameter of 15 ± 5 nm (Figure S11, Supporting Information). The measured I - V characteristics are shown in Figure 4c (see the Experimental Section for details). The osmotic current I_o and the osmotic potential V_o were obtained using a standard procedure.^[39]

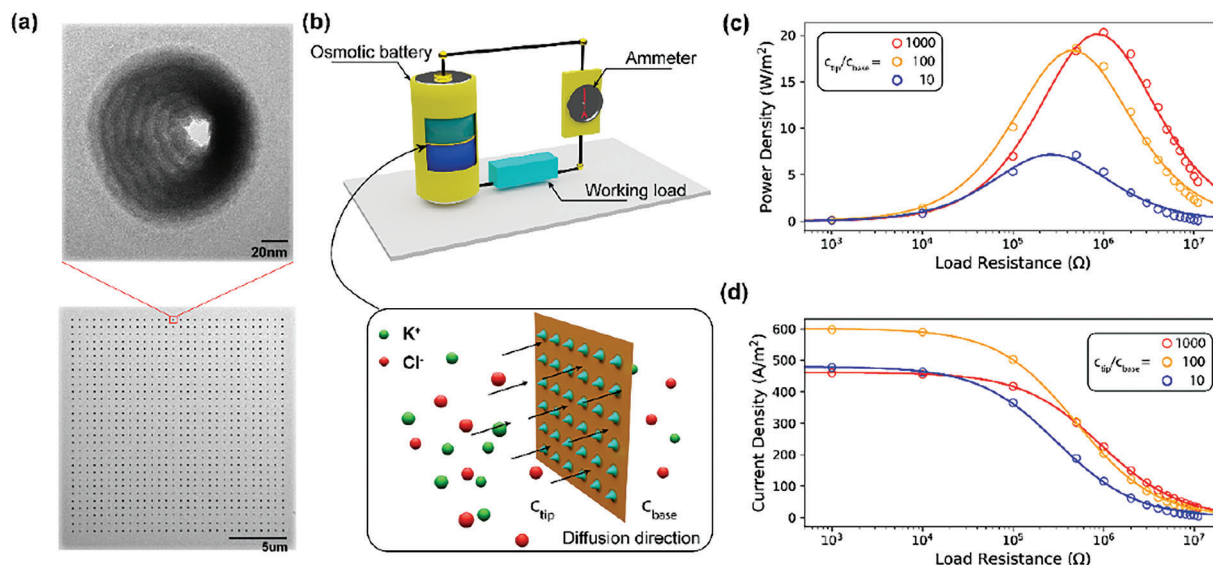


Figure 5. Osmotic power generation with an array of stalactite nanopores. a) Single HfO_2 stalactite conical nanopore (TEM image, top) out of an array of $30 \times 30 = 900$ stalactite conical nanopores (TEM image, bottom) on a $400 \mu\text{m}^2$ surface of a freestanding SiN membrane. The pores have a base of 100 ± 5 nm and a tip of 18 ± 5 nm, analyzed from random 13 positions in the arrays (Figure S13, Supporting Information). b) Osmotic power generation setup layout (top), and 3D representation of the membrane (bottom). Arrows show the direction of the current flow from high to low salt concentration. c,d) Measured power and current density, respectively, for the tip-to-base direction of the concentration gradient. Three curves are for the concentration of 0.1 M (blue), 0.01 M (yellow), and 0.001 M (red) on the low-concentration side. The concentration of the high-concentration side is fixed and equal to 1 M. All the curves are measured at $\text{pH} \approx 5$.

The tip-to-base flow direction showed higher V_o and I_o than the base-to-tip flow (Figure 4d). This effect originates from the difference in the spatial charge distribution (Figure 4e) for the two cases. Different ion rectification of the stalactite nanopore occurs due to the differential diffusion of cations and anions across the membrane in the presence of the concentration gradient. The difference between the values of osmotic current (left) and osmotic potential (right) for the tip-to-base and base-to-tip directions of the concentration gradients comes from the asymmetric geometry. The lower concentration at the base side leads to a broader electrical double layer (EDL) at the inner pore wall (Figure 4e left), which results in higher ion selectivity of the pore. The lower concentration on the tip side also yields a widening of EDL, but on the flat substrate side only. As a result, the electric field distribution inside the pore is not perturbed, and the selectivity drops. Thus, geometric asymmetry provides additional benefits for the osmotic energy conversion compared to the cylindrical nanopores. The surface charges at the pore walls can vary by surface modification. This treatment can additionally increase the efficiency of osmotic power generation.

Figure 4f shows the dependence of I_o on concentration gradients. Three curves are measured at different pH and show a high sensitivity of the osmotic current on the surface charge, which is known to be pH dependent.^[40] Although the highest osmotic current is observed for $\text{pH} = 9$, the HfO_2 nanopore shows comparatively good osmotic power at neutral pH. This fact positively distinguishes our assembly as it can be used for natural applications, such as energy harvesting at the sea-river contact in which water has neutral pH. Our experiment showed that a single conical HfO_2 nanopore generates 0.4 nW of power at $\text{pH} = 5$ and 1 nW at $\text{pH} = 9$. These values are higher compared to

the previously reported for nanofluidic systems.^[39,41] Moreover, stalactite nanopores are very stable due to the inert chemical nature of HfO_2 . Our nanopores showed excellent stability in 1 M KCl solution for 42 days. The variation of pore conductance was within 10% (Figure S12, Supporting Information). Modifying the surface of our HfO_2 nanopore by deposition of superhydrophobic materials can also further increase the efficiency of osmotic power generation.

3.4. Osmotic Energy Conversion with Nanopore Arrays

Practical applications, such as osmotic power generation, energy storage, filtration, and separation, require high throughput and, thus, arrays of nanopores rather than a single pore.^[19,42,43] To demonstrate the scaling potential of stalactite nanopores, we used templated silicon nitride aperture arrays with 900 nanopores (Figure 5a bottom) at which HfO_2 was grown by the same procedure as for a single pore. Arrays consisted of the equivalent single pores of 15 ± 5 nm (Figure 5a top). We found that the transition from a single pore to an array does not affect the precision of the fabrication and quality of the nanopores.

Figure 5b shows the experimental setup layout. It consists of the osmotic battery with the nanopore membrane, the ammeter, and the imitation of the working load. We used a tip-to-base concentration gradient direction that showed a higher osmotic current on a single pore (Figure 4). Note the device showed a remarkably high output current stability for more than one hour under a 1–0.1 M KCl concentration gradient (Figure S14, Supporting Information). Varying the load resistance, we measured the device power density (Figure 5c) and the current density (Figure 5d) for

three different salinity gradients. The device showed the highest power density at $c_{\max}/c_{\min} = 10^3$ and a load resistance of 1 m Ohm. Taking into account the membrane surface of $400 \mu\text{m}^2$, we acquire 20 W m^{-2} from this demonstration device. The HfO_2 pores permit the deposition of any materials on their surface by an additional standard atomic-layer deposition technique, which is a cheap method for surface modification. Further studies in this direction can improve the functional properties of our stalactite nanopores' surface charge.

4. Conclusion

We demonstrated a nature-inspired controllable fabrication method of the stalactite nanopores made by the self-assembled anisotropic growth of HfO_2 shallow nanostructure on templated silicon nitride apertures. By tuning the diameter of templated silicon nitride apertures and the number of cycles of precursor supply, we demonstrated nanopore devices with a tunable diameter from single-digit to several hundreds of nanometers. TEM imaging and EDX mapping confirmed the selective growth of HfO_2 stalactite-like structures inside silicon nitride apertures, which differs from the standard ALD. We showed that nanoconfinement enhances the local growth rate by two orders of magnitude compared to the conventional ALD process. Among these two directions from the asymmetric structure, the advantage of tip-to-base direction in our asymmetric stalactite nanopores has been demonstrated through DNA translocation and reversed electro-dialysis. Both experiments demonstrated better DNA capture and osmotic energy conversion efficiency for the tip-to-base direction of the concentration gradient. Using the array of $400 \mu\text{m}^2$ with 900 nanopores, we demonstrated an efficient osmotic power generation. Due to the extremely inert nature of HfO_2 , the device degradation rate was found to be less than 10% per month, which provides state-of-the-art stability suitable for real-life applications. The pores can be further modified by standard ALD material deposition to obtain the optimal diameter and surface charge for a target application. The proposed method provides a new adaptable platform in terms of geometry and material composition for applied and basic nanofluidic research, including bioengineering, ionotronics, energy science, and filtration technologies.

5. Experimental Section

Sample Preparation: Standard 4-in. boron-doped $380 \pm 10 \mu\text{m}$ thick silicon (1–10 Ohm cm) wafers supplied by the EPFL Center of MicroNanoTechnology (CMI) was used. The layers of 60 nm of dry silicon oxide and 20 nm of low-stress silicon nitride were formed at the polished surfaces using Centrotherm furnaces at the CMI clean-room facility. The nanopores in the template were patterned by using e-beam lithography with consequent dry etching.^[44] Each wafer had either a single pore or an array of nanopores with the template apertures varying from 100 to 200 nm. To grow the hafnium-oxide “stalactite” at the orifice of the silicon nitride template aperture, a commercial BeneQ TFS200 ALD setup was used. To initiate the HfO_2 precipitation, two precursors were used: pure water vapor and 99.99% Tetrakis-(ethylmethylamido)-hafnium (IV), purchased from Sigma-Aldrich. The chamber temperature was set to 200 °C, and the precursors' temperature was set to 80 °C following the recipe described before.^[45] The precursors' injection was repeated several times to get the required number of rings of the stalactite. The chamber was purged with nitrogen for 2 s between the cycles. The growth rate for this recipe and

a standard flat surface was $1.01 \pm 0.05 \text{ \AA}$ per cycle. To heat the SiN template, the IncoX-316L substrate was used. Each sample was preheated for 15 min before the growth cycle. For the biomolecules translocation experiment, 2-kbp double-stranded DNA in 1 M aqueous solution of KCl was used.

Sample Characterization: The samples were imaged using Thermo Fisher OsirisT, Talos F200S, and Titan Themis Cubed TEM operated at 200 and 300 kV for the latter. The aberration-corrected Titan instrument was used for high-resolution imaging. Two different operating modes of the instruments were used: TEM for collecting the bright-field TEM micrographs and scanning TEM (STEM) for performing the energy-dispersive X-ray (EDX) spectroscopy mappings. The EDX atomic fraction mapping of the single nanopore (Figure 2b(III)) was obtained by Cliff-Lorimer quantification of the net count signal (Figure 2b(I) and (II)) with all the elements in the presence (N, O, Si, and Hf) using Velox software. To observe the “side view” of the stalactite nanostructure (Figure 2a(II)) the SiN membrane with the HfO_2 stalactite was cut perpendicularly to the wafer surface by Ga^+ ions using Zeiss Crossbeam 540 FIB-SEM system. Scanning electron microscopy images of the icicle-pore arrays (Figure 1b) were obtained at 1.5 kV.

Numerical Simulations: To visualize the ions distribution and the electric field distribution within the icicle nanopores, the COMSOL Multiphysics package was used. The electric field distribution was simulated using the finite element method (FEM). The calculations were made in a stationary regime with stalactite nanopore dimensions measured in the STEM micrographs. The electric field distribution was calculated in different concentration conditions used in the real DNA translocation and reverse-electrodialysis (RED) experiments detailed in the Supporting Information.

Data Collection and Statistical Analysis: In the reversed electro-dialysis experiment of HfO_2 nanopore, the ionic current signal is sampled by Axon Patch 200B or Femto DLPCA-200. All the osmotic current and voltage is an average value from at least three times of experimental repetition. In DNA sensing section, the ionic currents were recorded using Axopatch 200B (Axon Instruments, USA) low-pass filtered at 100 kHz using a built-in Bessel low-pass filter and sampled at a 200 kHz sampling rate. The translocation data analysis, event detection, and plotting were done using the Python-based OpenNanopore toolkit (<https://www.epfl.ch/labs/lben/opennanopore-python>).

Supporting Information

Supporting Information is available from the Wiley Online Library or from the author.

Acknowledgements

The authors acknowledge the financial support from the Swiss National Science Foundation through the National Centre of Competence in Research Bio-Inspired Materials and Grant No. 200021_192037. A.C. acknowledged Bridge POC grant by SNF and Innosuisse (Grant No. 40B1-0_205841 Nano-IonEX membrane). Y.T. acknowledged UCAS Joint PhD Training Program. The authors would like to thank the EPFL Center of MicroNanoTechnology (CMI) for their help with chip fabrication and the EPFL Center for Electron Microscopy (CIME) for access to electron microscopes. They also would like to thank Dr. Lihter and Dr. Navikas for their artistic representation of the stalactite nanopore.

Open access funding provided by Ecole Polytechnique Federale de Lausanne.

Conflict of Interest

The authors declare that they have filed a patent related to the work presented in this manuscript.

Author Contributions

A.C. and Y.T. contributed equally to this work. A.C., Y.T., and A.R. conceived the idea and designed the study. A.C. and Y.T. fabricated the HfO₂ stalactite nanopore substrates. A.C., Y.T., and M.T. performed the experiments. Y.T. performed finite element analysis. V.B. and L.N. performed aberration-corrected TEM and FIB-milling of the nanopore substrates, respectively. A.C., Y.T., M.T., and V.A. wrote the manuscript. N.C., V.A., and T.-H. C. contributed to the discussion on the applications of the HfO₂ stalactite nanopore. V.A. and L.W. contributed to the discussion on osmotic energy conversion. A.R. supervised the work. All authors contributed to the writing and discussion of the manuscript.

Data Availability Statement

The data that support the findings of this study are available from the corresponding author upon reasonable request.

Keywords

asymmetric structure, DNA sensing, nanofluidics, osmotic energy conversion, solid-state nanopore, thin film deposition

Received: March 27, 2023

Revised: May 24, 2023

Published online:

- [1] J. J. Kasianowicz, E. Brandin, D. Branton, D. W. Deamer, *Proc. Natl. Acad. Sci. USA* **1996**, *93*, 13770.
- [2] D. Stein, M. Kruithof, C. Dekker, *Phys. Rev. Lett.* **2004**, *93*, 035901.
- [3] C. Dekker, *Nat. Nanotechnol.* **2007**, *2*, 209.
- [4] Y. Teng, P. Liu, L. Fu, X.-Y. Kong, L. Jiang, L. Wen, *Proc. Natl. Acad. Sci. USA* **2020**, *117*, 16743.
- [5] R. A. Lucas, C.-Y. Lin, L. A. Baker, Z. S. Siwy, *Nat. Commun.* **2020**, *11*, 1568.
- [6] P. Robin, T. Emmerich, A. Ismail, A. Niguès, Y. You, G.-H. Nam, A. Keerthi, A. Siria, A. K. Geim, B. Radha, L. Bocquet, *Science* **2023**, *379*, 161.
- [7] L. Xue, H. Yamazaki, R. Ren, M. Wanunu, A. P. Ivanov, J. B. Edel, *Nat. Rev. Mater.* **2020**, *5*, 931.
- [8] E. T. Acar, S. F. Buchsbaum, C. Combs, F. Fornasiero, Z. S. Siwy, *Sci. Adv.* **2019**, *5*, eaav2568.
- [9] A. Fang, K. Kroenlein, D. Riccardi, A. Smolyanitsky, *Nat. Mater.* **2019**, *18*, 76.
- [10] L. Bocquet, *Nat. Mater.* **2020**, *19*, 254.
- [11] B. Cressiot, S. J. Greive, M. Mojtavavi, A. A. Antson, M. Wanunu, *Nat. Commun.* **2018**, *9*, 4652.
- [12] A. R. Hall, A. Scott, D. Rotem, K. K. Mehta, H. Bayley, C. Dekker, *Nat. Nanotechnol.* **2010**, *5*, 874.
- [13] J. Larkin, R. Henley, D. C. Bell, T. Cohen-Karni, J. K. Rosenstein, M. Wanunu, *ACS Nano* **2013**, *7*, 10121.
- [14] H. Yamazaki, R. Hu, Q. Zhao, M. Wanunu, *ACS Nano* **2018**, *12*, 12472.
- [15] Y.-C. Chou, P. Masih Das, D. S. Monos, M. Drndić, *ACS Nano* **2020**, *14*, 6715.
- [16] M. Thakur, N. Cai, M. Zhang, Y. Teng, A. Chernev, M. Tripathi, Y. Zhao, M. Macha, F. Elharouni, M. Lihter, L. Wen, A. Kis, A. Radenovic, *npj 2D Mater. Appl.* **2023**, *7*, 11.
- [17] Y. He, M. Tsutsui, Y. Zhou, X.-S. Miao, *NPG Asia Mater* **2021**, *13*, 48.
- [18] H. Liu, Q. Zhou, W. Wang, F. Fang, J. Zhang, *Small* **2023**, *19*, 2205680.
- [19] A. Gadaleta, C. Sempere, S. Gravelle, A. Siria, R. Fulcrand, C. Ybert, L. Bocquet, *Phys. Fluids* **2014**, *26*, 012005.
- [20] L. Ma, Z. Li, Z. Yuan, C. Huang, Z. S. Siwy, Y. Qiu, *Anal. Chem.* **2020**, *92*, 16188.
- [21] M. Macha, S. Marion, V. V. R. Nandigana, A. Radenovic, *Nat. Rev. Mater.* **2019**, *4*, 588.
- [22] N. K. Katiyar, G. Goel, S. Hawi, S. Goel, *NPG Asia Mater.* **2021**, *13*, 56.
- [23] D. M. Black, *Sci. Mon.* **1952**, *74*, 206.
- [24] R. S. Shaw, N. Packard, M. Schröter, H. L. Swinney, *Proc. Natl. Acad. Sci. USA* **2007**, *104*, 9580.
- [25] Z. Zhang, X. Sui, P. Li, G. Xie, X.-Y. Kong, K. Xiao, L. Gao, L. Wen, L. Jiang, *J. Am. Chem. Soc.* **2017**, *139*, 8905.
- [26] J.-P. Hsu, T.-C. Su, P.-H. Peng, S.-C. Hsu, M.-J. Zheng, L.-H. Yeh, *ACS Nano* **2019**, *13*, 13374.
- [27] X. Liu, M. M. Skanata, D. Stein, *Nat. Commun.* **2015**, *6*, 6222.
- [28] K. J. Freedman, L. M. Otto, A. P. Ivanov, A. Barik, S.-H. Oh, J. B. Edel, *Nat. Commun.* **2016**, *7*, 10217.
- [29] N. A. W. Bell, M. Muthukumar, U. F. Keyser, *Phys. Rev. E* **2016**, *93*, 022401.
- [30] L. Luo, D. A. Holden, H. S. White, *ACS Nano* **2014**, *8*, 3023.
- [31] M. Wanunu, W. Morrison, Y. Rabin, A. Y. Grosberg, A. Meller, *Nat. Nanotechnol.* **2010**, *5*, 160.
- [32] M. Muthukumar, *J. Chem. Phys.* **2010**, *132*, 195101.
- [33] S. W. Kowalczyk, D. B. Wells, A. Aksimentiev, C. Dekker, *Nano Lett.* **2012**, *12*, 1038.
- [34] N. A. W. Bell, K. Chen, S. Ghosal, M. Ricci, U. F. Keyser, *Nat. Commun.* **2017**, *8*, 380.
- [35] N. M. Fahrenkopf, P. Z. Rice, M. Bergkvist, N. A. Deskins, N. C. Cady, *ACS Appl. Mater. Interfaces* **2012**, *4*, 5360.
- [36] S. Carson, J. Wilson, A. Aksimentiev, M. Wanunu, *Biophys. J.* **2014**, *107*, 2381.
- [37] A. Fragasso, S. Schmid, C. Dekker, *ACS Nano* **2020**, *14*, 1338.
- [38] Z. Zhang, L. Wen, L. Jiang, *Nat. Rev. Mater.* **2021**, *6*, 622.
- [39] J. Feng, M. Graf, K. Liu, D. Ovchinnikov, D. Dumcenco, M. Heiranian, V. Nandigana, N. R. Aluru, A. Kis, A. Radenovic, *Nature* **2016**, *536*, 197.
- [40] C. Lee, L. Joly, A. Siria, A.-L. Biance, R. Fulcrand, L. Bocquet, *Nano Lett.* **2012**, *12*, 4037.
- [41] A. Siria, P. Poncharal, A.-L. Biance, R. Fulcrand, X. Blase, S. T. Purcell, L. Bocquet, *Nature* **2013**, *494*, 455.
- [42] K. Yazda, K. Bleau, Y. Zhang, X. Capaldi, T. St-Denis, P. Grutter, W. W. Reisner, *Nano Lett.* **2021**, *21*, 4152.
- [43] M. Tsutsui, K. Yokota, I. W. Leong, Y. He, T. Kawai, *Cell Rep. Phys. Sci.* **2022**, *3*, 101065.
- [44] M. Thakur, M. Macha, A. Chernev, M. Graf, M. Lihter, J. Deen, M. Tripathi, A. Kis, A. Radenovic, *Small Methods* **2020**, *4*, 2000072.
- [45] D. M. Hausmann, E. Kim, J. Becker, R. G. Gordon, *Chem. Mater.* **2002**, *14*, 4350.